

CHARACTERIZING THE PRESSURE SMOOTHING SCALE OF THE INTERGALACTIC MEDIUM

GIRISH KULKARNI^{1,2}, JOSEPH F. HENNAWI², JOSE OÑORBE², ALBERTO RORAI^{1,2}, VOLKER SPRINGEL^{3,4}*Draft version August 6, 2018*

ABSTRACT

The thermal state of the intergalactic medium (IGM) at $z < 6$ constrains the nature and timing of cosmic reionization events, but its inference from the Ly α forest is degenerate with the 3-D structure of the IGM on ~ 100 kpc scales, where, analogous to the classical Jeans argument, the pressure of the $T \simeq 10^4$ K gas supports it against gravity. We simulate the IGM using smoothed particle hydrodynamics, and find that, at $z < 6$, the gas density power spectrum does not exhibit the expected filtering scale cutoff, because dense gas in collapsed halos dominates the small-scale power masking pressure smoothing effects. We introduce a new statistic, the real-space Ly α flux, F_{real} , which naturally suppresses dense gas, and is thus robust against the poorly understood physics of galaxy formation, revealing pressure smoothing in the diffuse IGM. The F_{real} power spectrum is accurately described by a simple fitting function with cutoff at λ_F , allowing us to rigorously quantify the pressure smoothing scale for the first time: we find $\lambda_F = 79$ kpc (comoving) at $z = 3$ for our fiducial thermal model. This statistic has the added advantage that it directly relates to observations of correlated Ly α forest absorption in close quasar pairs, recently proposed as a method to measure the pressure smoothing scale. Our results enable one to quantify the pressure smoothing scale in simulations, and ask meaningful questions about its dependence on reionization and thermal history. Accordingly, the standard description of the IGM in terms of the amplitude T_0 and slope γ of the temperature-density relation $T = T_0(\rho/\bar{\rho})^{\gamma-1}$ should be augmented with a third pressure smoothing scale parameter λ_F .

Subject headings: dark ages, reionization, first stars – galaxies: high-redshift – intergalactic medium – large-scale structure of the universe – quasars: absorption lines

1. INTRODUCTION

The intergalactic medium (IGM) is a rich repository of cosmic history. It contains most of the mass of the universe and records a variety of baryonic and non-baryonic processes that occur as the universe evolves (Meiksin 2009). This makes the IGM a valuable cosmological laboratory for testing models of structure formation. The most readily observable probe of the IGM is the Ly α forest, the collection of absorption lines seen at redshifts $z \sim 2-5$ in spectra of high-redshift quasars. Hydrodynamical simulations of structure formation in a Λ CDM universe show that the Ly α forest results from the interaction between a background of UV photons created by active galactic nuclei (AGN) and star-forming galaxies, and fluctuations in gas density sourced by gravitational instability (Cen et al. 1994; Hernquist et al. 1996; Zhang et al. 1997; McDonald et al. 2000; Meiksin et al. 2001; Croft et al. 2002; Viel et al. 2004; Lukić et al. 2015). This picture successfully explains several statistical properties of the Ly α forest, such as the H I column density distribution, and the line-of-sight power spectrum and probability density function (PDF) of the transmitted flux.

The Ly α forest can be used to probe the evolution of the thermal state of the IGM at redshifts $z \sim 2-5$. On cosmological time scales, the thermal state of the IGM is

expected to evolve through four stages (e.g., Barkana & Loeb 2001; Pritchard & Loeb 2012): (1) Between recombination ($z \sim 1100$) and $z = 147$, the cosmic gas temperature is coupled to the cosmic microwave background (CMB) temperature via Compton scattering off a small fraction of residual free electrons. As a result the gas temperature falls as $T_{\text{gas}} \propto (1+z)$ from $T_{\text{gas}} \gtrsim 10^3$ K at recombination to $T_{\text{gas}} \sim 400$ K at $z = 147$. (2) At lower redshifts ($z < 147$), the free electron fraction is no longer sufficient to couple gas and CMB temperatures, and gas cools adiabatically as $T_{\text{gas}} \propto (1+z)^2$ down to $T_{\text{gas}} \sim 2$ K at $z = 10$. (3) As galaxies start forming at $z = 10$, UV radiation from young, massive stars and possibly a population of faint AGN deposits large amount of energy in the IGM on time scales of ~ 500 Myr. In this relatively short period of time—the “epoch of hydrogen reionization”—most of the H I and He I content of the IGM is ionized to H II and He II respectively. This also heats the IGM via photoionization heating so that by $z \sim 6$ the IGM temperature is $T_{\text{gas}} \sim 10^4$ K (Bolton et al. 2010, 2012). (4) Due to the small neutral hydrogen fraction ($x_{\text{HI}} \sim 10^{-4}$) in the IGM at the end of the epoch of hydrogen reionization, UV photons can propagate through the IGM to large distances without absorption. As a result, a UV background is established. The IGM remains in ionization equilibrium with this background and begins to cool as the Universe expands. However, AGN activity peaks at $z \sim 3$, resulting in an abundance of hard photons that ionize He II to He III and likely reheats the IGM to higher temperatures. This “epoch of helium reionization” probably ends at $z \sim 2.7$ (Shull et al. 2010; Worseck et al. 2011; Syphers & Shull 2013; Worseck et al. 2014) after which the IGM is again expected to cool down to the

¹ Institute of Astronomy and Kavli Institute of Cosmology, University of Cambridge, Madingley Road, Cambridge CB3 0HA, UK; kulkarni@ast.cam.ac.uk

² Max Planck Institute for Astronomy, Königstuhl 17, D-69117 Heidelberg, Germany

³ Heidelberg Institute for Theoretical Studies, Schloss-Wolfsbrunnengasse 35, D-69118 Heidelberg, Germany

⁴ Zentrum für Astronomie der Universität Heidelberg, ARI, Mönchhofstr. 12-14, D-69120 Heidelberg, Germany

present epoch. By studying the Ly α forest one can constrain the thermal state of the IGM providing insights into the Universe's thermal history.

It is well known that the balance between cooling due to Hubble expansion and heating due to the gravitational collapse and photoionization heating give rise to a well-defined temperature-density relationship in the IGM (Hui & Gnedin 1997)⁵, which can be written as

$$T = T_0 \left(\frac{\rho}{\bar{\rho}} \right)^{\gamma-1}, \quad (1)$$

where T_0 is the temperature at the mean density $\bar{\rho}$. Immediately after the reionization of H I ($z < 6$) or He II ($z < 3$), T_0 is likely to be around 2×10^4 K and $\gamma \sim 1$ (Hui & Gnedin 1997). At lower redshifts, T_0 decreases adiabatically while γ is expected to increase and asymptotically approach a value of 1.62 (Hui & Gnedin 1997). The remarkable fact that the mean temperature-density relation of the baryons in the IGM can be well approximated by a simple power law is behind the standard observational approach of measuring the thermal state of the IGM from the Ly α forest: statistical properties of the forest are measured and compared to hydrodynamical simulations to constrain T_0 and γ . Statistics considered for this purpose are line-of-sight power spectrum of transmitted flux (Zaldarriaga et al. 2001; Viel et al. 2009), PDF of wavelet amplitudes in a wavelet decomposition of the forest (Theuns & Zaroubi 2000; Theuns et al. 2002b; Lidz et al. 2010; Garzilli et al. 2012), the average local curvature of the spectrum (Becker et al. 2011; Boera et al. 2014), PDF of transmitted flux values (McDonald et al. 2001; Kim et al. 2007; Bolton et al. 2008; Calura et al. 2012; Garzilli et al. 2012; Lee et al. 2015), and the slope of the b -parameter distribution (Haehnelt & Steinmetz 1998; Theuns et al. 2000; Ricotti et al. 2000; Bryan & Machacek 2000; Schaye et al. 2000; McDonald et al. 2001; Theuns et al. 2002a; Rudie et al. 2012; Bolton et al. 2014).

However, these measurements rely on the longitudinal, one-dimensional, structure of the Ly α forest, which is also influenced by the three-dimensional pressure smoothing. At large scales and low densities, baryons in the IGM are expected to follow the underlying dark matter distribution. However, at small scales and high densities, baryons experience pressure forces that prevent them from tracing the collisionless dark matter. This pressure results in an effective three-dimensional smoothing of the baryon distribution relative to the dark matter, at a characteristic scale known as the pressure smoothing scale. This pressure smoothing affects absorption lines in the Ly α forest by reducing power in the distribution of H I at scales smaller than the pressure smoothing scale. This effect, which reduces the small-scale power in the longitudinal transmitted flux power spectrum, is degenerate with a similar but one-dimensional reduction due to thermal broadening (Peeples et al. 2010a,b; Rorai et al. 2013; Garzilli et al. 2015).

This degeneracy has been largely ignored by previous measurements of the IGM temperature, all of which use

line-of-sight information from the Ly α forest (but see Becker et al. (2011) and Puchwein et al. (2014)). As a result, published constraints on T_0 and γ are confusing and sometimes contradictory. For example, measurements of γ do not agree with each other; some measurements even suggest an inverted temperature-density relation ($\gamma < 1$), which is difficult to obtain in canonical IGM models (Bolton et al. 2008; Viel et al. 2009; Calura et al. 2012; Garzilli et al. 2012).⁶ Consequently, an important goal of IGM studies is to break this degeneracy and bring robustness to measurements of the thermal state of the IGM.

The degeneracy can be broken by a suitable transverse measurement that is sensitive only to pressure smoothing. Rorai et al. (2013) showed that this can be achieved by measuring coherence of Ly α forest absorption in close quasar pairs. Spectra of close quasar pairs will become increasingly coherent as the transverse separation between the quasars approaches the pressure smoothing scale. Rorai et al. (2013) demonstrated that this effect can be exploited by measuring the probability distribution function of phase angle differences between homologous line-of-sight Fourier modes in quasar pair spectra. This new technique has tremendous promise for direct measurements of the pressure smoothing scale, and Rorai et al. (2013) showed that applying it to a realistic data set should yield measurements with 5% precision.

The precision with which quasar pair measurements will be able to characterize the pressure smoothing scale motivates us to better understand pressure smoothing in the IGM. Classically, a simple characterization of the pressure smoothing scale is given by (Binney & Tremaine 2008)

$$\lambda_{F, \text{Jeans}}^2(t) = \frac{c_s^2(t)a(t)}{4\pi G \bar{\rho}_{m0}}, \quad (2)$$

in comoving units, where $\bar{\rho}_{m0}$ is the average comoving matter density, a is the cosmological scale factor, and c_s is the sound speed. Thus the pressure smoothing scale is a function of the instantaneous gas temperature. Nevertheless, in an expanding universe with an evolving thermal state, the pressure smoothing scale at a given epoch is expected to depend on the entire thermal history, because fluctuations at earlier times expand or fail to collapse depending on the IGM temperature at that epoch. In the limit of linear density perturbations, an analytical estimate of the dependence of the pressure smoothing scale on thermal history can be obtained (Gnedin & Hui 1998). The resultant pressure smoothing scale, termed filtering scale, can be written as

$$\lambda_{F, \text{GH98}}^2(t) = \frac{4\pi G \bar{\rho}_{m0}}{b(t)} \int_0^t dt' \frac{b(t') \lambda_{F, \text{Jeans}}^2(t')}{a(t')} \times \int_{t'}^t \frac{dt''}{a^2(t'')}, \quad (3)$$

in comoving units, where $\bar{\rho}_{m0}$ is the average comoving matter density, b is the growth factor of linear perturbations, and $\lambda_{F, \text{Jeans}}$ is given by Equation (2). Note that the filtering scale $\lambda_{F, \text{GH98}}$ is larger than $\lambda_{F, \text{Jeans}}$ before reionization, and smaller than $\lambda_{F, \text{Jeans}}$ (typically

⁵ The temperature-density relation is often also called the effective equation of state of the IGM. The thermodynamic equation of state is that of an ideal gas.

⁶ This can however be achieved in more exotic models such as TeV blazar heating (Chang et al. 2012; Puchwein et al. 2012).

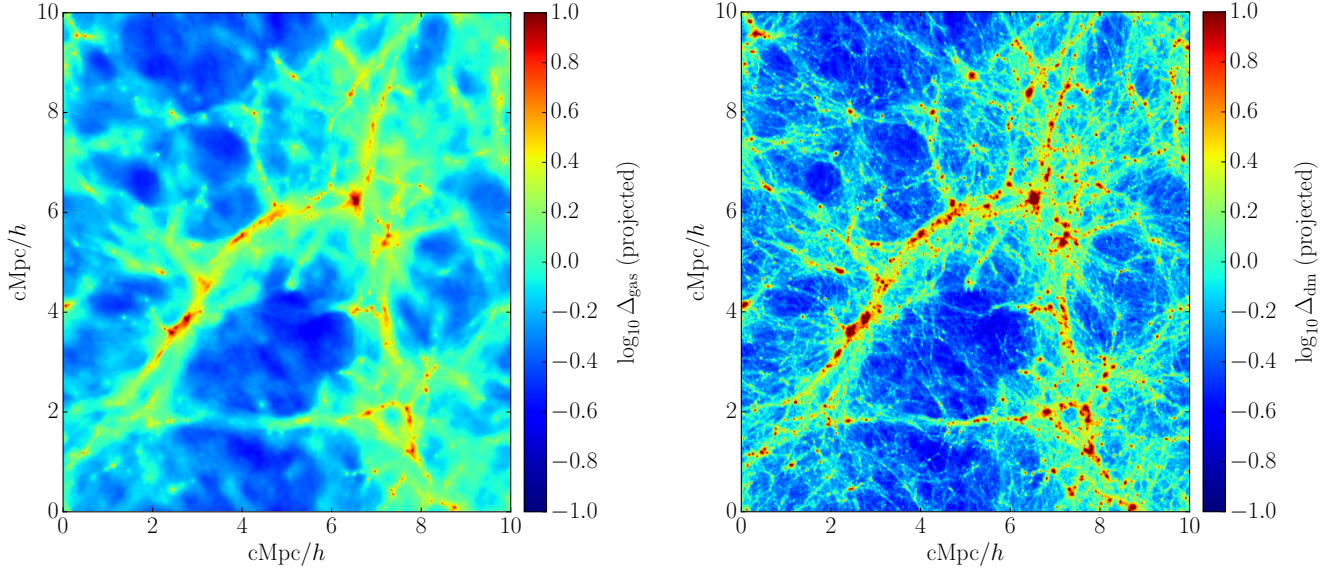


Figure 1. Projected density distributions of gas (left) and dark matter (right) at $z = 3$ in our fiducial simulation, showing pressure smoothing of gas relative to dark matter. The density at each point is an average for a column approximately 5 Mpc/h long.

by about a factor of 2) after reionization. At redshifts probed by the Ly α forest, typical values of $\lambda_{F,GH98}$, assuming simple models for the IGM thermal state, are about a hundred comoving kiloparsecs. With this filtering scale in hand, it is usually assumed that baryonic density is given by the dark matter density smoothed by a quadratic (Bi & Davidsen 1997) or a Gaussian kernel (Gnedin et al. 2003; Rorai et al. 2013) with width $\lambda_{F,GH98}$.

However, this description of the pressure smoothing in the IGM suffers from two problems. First, scales comparable to the pressure smoothing scale, i.e., scales of order hundreds of comoving kpc, are highly nonlinear at redshifts $z \sim 2-5$ probed by the Ly α forest. Therefore, the above linear perturbation theory description of λ_F breaks down at these redshifts. This means that the dependence of the IGM pressure smoothing scale on the thermal history is likely more complicated than Equation (3). Secondly, it is unclear that pressure smoothing of the baryons can be well described as Gaussian or quadratic smoothing of underlying dark matter density, because at scales of ~ 100 comoving kiloparsecs, galaxy formation physics could significantly influence the baryon distribution. Both of these limitations will affect the interpretation of the pressure smoothing scale from observations of the Ly α forest. The goal of this paper is to shed light on the pressure smoothing scale of the IGM using high-resolution hydrodynamical simulations. We ask if the pressure smoothing in the IGM is well described by the approximations in Equations (2) and (3), and present an improved characterization of the pressure smoothing scale.

The structure of this paper is as follows: In Section 2 we review the quadratic and Gaussian descriptions of the IGM and the motivations behind them. We present our simulations in Section 3. We analyze our numerical results and present a new characterization of the IGM pressure smoothing scale in Section 4. Section 5 contains a summary of our main conclusions. We work with a

Λ CDM cosmological model with $\Omega_b = 0.045$, $\Omega_m = 0.26$, $\Omega_\Lambda = 0.73$, $h = 0.71$, $n = 0.96$, $\sigma_8 = 0.80$ (Hinshaw et al. 2013). All distances are in comoving units.

2. ANALYTICAL ESTIMATES

In this section, we review the linear theory results that are traditionally used to describe the pressure smoothing scale of the IGM. The IGM is conventionally described as an ideal gas with a polytropic equation of state, $p = K\rho^{5/3}$. Then, in comoving coordinates, linear evolution of density perturbations is given by

$$\begin{aligned} \frac{d^2\delta_b}{dt^2} + 2H\frac{d\delta_b}{dt} &= 4\pi G(\bar{\rho}_b\delta_b + \bar{\rho}_m\delta_m) - \frac{c_s^2}{a^2}k^2\delta_b, \\ \frac{d^2\delta_m}{dt^2} + 2H\frac{d\delta_m}{dt} &= 4\pi G(\bar{\rho}_b\delta_b + \bar{\rho}_m\delta_m), \end{aligned} \quad (4)$$

where $\delta_b(t, \mathbf{k})$ and $\delta_m(t, \mathbf{k})$ are Fourier amplitudes of baryon and dark matter density contrasts ($\delta \equiv \rho/\bar{\rho} - 1$) respectively and $\bar{\rho}_b, \bar{\rho}_m \propto a^{-3}$. The ratio $\delta_b(t, \mathbf{k})/\delta_m(t, \mathbf{k})$ will reveal the pressure smoothing scale k_F at which pressure support equals gravitational force.

2.1. Linear evolution for an adiabatic thermal history

We can ignore $\bar{\rho}_b$ relative to $\bar{\rho}_m$ in the gravitational source term on the right hand sides of Equations (4). The dark matter evolution can then be solved as usual to obtain the growing mode $b(z)$ (Peebles 1980). For baryonic perturbations, a general solution can be obtained at $z > 2$ where $b \sim a$, if we assume that the temperature at the mean density, T_0 evolves as $1/a$ (Bi et al. 1992). This solution can be written as

$$\frac{\delta_b(t, \mathbf{k})}{\delta_m(t, \mathbf{k})} = \frac{1}{1 + \lambda_J^2 k^2}, \quad (5)$$

where we have only retained the growing mode. The parameter λ_J is defined as

$$\lambda_J^2 = \frac{c_s^2}{4\pi G \bar{\rho}_m a^2}, \quad (6)$$

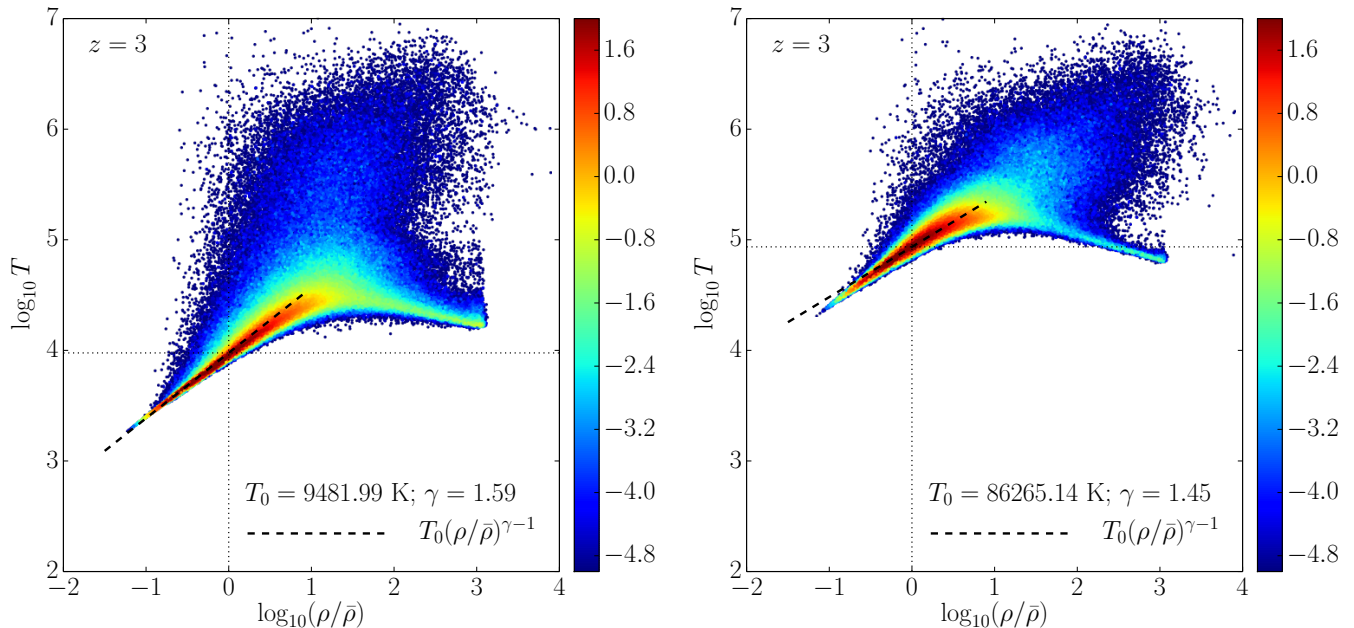


Figure 2. Comparison of the phase-space distributions of gas particles in two of the simulations presented in this paper. (Left panel describes the fiducial simulation.) Color scale describes density of points on the plot; most particles are on the temperature-density relation shown by the dashed black line.

which is just the classical Jeans scale of Equation (2). Due to Equation (6), for a polytropic IGM, the assumption that $T_0 \propto 1/a$ results in a constant λ_J at all times. Equation (5) describes the behavior of baryons relative to the dark matter to linear order in δ_b , at redshifts $z > 2$, under the assumption that $T_0 \propto 1/a$. It shows that, in linear theory, baryonic density fluctuations are damped relative to the dark matter fluctuations by a quadratic filter $1 + \lambda_J^2 k^2$. At large scales ($k \ll \lambda_J$), baryons follow the dark matter ($\delta_b = \delta_m$) but at small scales ($k \gg \lambda_J$), baryons are smoothed out by pressure support ($\delta_b = \delta_m / \lambda_J^2 k^2$).⁷

2.2. Linear evolution for an arbitrary thermal history

However, as discussed in Section 1 above, in general the thermal history of the IGM is expected to be different from $T \propto 1/a$. For example, T is expected to increase during cosmic reionization events, and additionally photoionization heating due to the UV background will generally result in different temperature evolution. In general, for an arbitrary thermal history $T(a)$ a generalization of Equation (5) cannot be obtained analytically. But an approximate result can be derived to first order in k^2 , i.e., at large scales (Gnedin & Hui 1998). This solution can be written as

$$\frac{\delta_b(t, \mathbf{k})}{\delta_m(t, \mathbf{k})} = 1 - k^2 \lambda_F^2, \quad (7)$$

⁷ A somewhat more general solution can be obtained for Equations (4) by assuming $T_0 \propto a^{-\alpha}$, which corresponds to a power law evolution of λ_J (Bi et al. 1992). (The above analysis corresponds to $\alpha = 1$). However, this solution has the same asymptotic behavior as Equation (5). Thus the quadratic filter in Equation (5) is a general feature of power law adiabatic thermal histories in the linear approximation.

where

$$\lambda_F^2 = \frac{4\pi G \bar{\rho}_{m0}}{b(t)} \int_0^t dt' \frac{b(t') \lambda_J^2(t')}{a(t')} \int_{t'}^t \frac{dt''}{a^2(t'')}, \quad (8)$$

in which the thermal history enters via λ_J and $\bar{\rho}_{m0}$ is the average matter density at $z = 0$ (recall that λ_J is defined in Equation (6)). Note that this describes the linear theory evolution of the IGM for an arbitrary thermal history only at large scales ($k^2 \lambda_F^2 \ll 1$). A closed-form solution of Equations (4) to all orders of $k^2 \lambda_F^2$ is not known. However, by solving Equations (4) numerically, Gnedin et al. (2003) show that the full solution is described to a good accuracy by a Gaussian of the form

$$\frac{\delta_b(t, \mathbf{k})}{\delta_m(t, \mathbf{k})} = \exp(-k^2 \lambda_F^2), \quad (9)$$

where λ_F is defined in Equation (8). Note that this solution describes the density fields only in the limit of linear perturbations. Typically, Equation (9) predicts a pressure smoothing scale of $\lambda_F \sim 100$ kpc (Gnedin & Hui 1998).

2.3. Nonlinear evolution

Equations (5) and (9) describe pressure smoothing of the baryons in the linear perturbation theory regime, i.e., in the limit of small density ($\delta < 1$). The generalization of these results to the nonlinear limit is unknown. By arguing that the Ly α forest is only sensitive to moderate overdensities ($\Delta \lesssim 10$), Equations (5) and (9) have been used in semi-analytical descriptions of the forest (Reisenegger & Miralda-Escudé 1995; Bi & Davidse 1997; Choudhury et al. 2001a,b). Several authors have also used these results to simulate the IGM using so-called pseudo-hydrodynamical methods (Petitjean et al. 1995; Gnedin & Hui 1998; Croft et al. 1998). In

terms of their predictions for simple cumulative statistics of absorption lines in the Ly α forest, these methods give results that are close to within 10% of hydrodynamical simulations (Meiksin & White 2001).

Nonetheless, the application of Equations (5) and (9) to characterize pressure smoothing at the scales and redshifts probed by the Ly α forest is problematic. Equations (5) and (9) typically predict pressure smoothing scales of order 100 kpc. At redshifts $z = 2$ –5, such small scales are highly nonlinear, as the variance in the density distribution at these scales is dominated by collapsed structures. Baryons at these densities are affected by the physics of galaxy formation, as well as gas outflows and inflows. Therefore, in order to understand pressure smoothing in the IGM, it would be necessary to somehow distinguish, at scales of ~ 100 kpc, the low density IGM that is likely unaffected by galaxy formation from the high density IGM that is affected by it. But where to draw the line between these two density regimes is not clear. Also, unlike in the linear regime ($\Delta < 1$), the pressure smoothing scale λ_F is expected to be dependent on the local density in the quasi-linear regime ($\Delta \lesssim 10$) probed by the Ly α forest, but this dependence is unknown, as the classical result of Equation (6) is not guaranteed to hold at densities of order 1–10. Therefore, even if the low density IGM is somehow isolated, we are still left with the task of characterizing its pressure smoothing.

In this paper we address these two issues, and present a method of isolating the low-density IGM in a way which enables characterization of the pressure smoothing scale that not only describes the pressure smoothing in the IGM, but also provides an important tool for interpreting pressure smoothing scale measurements from the Ly α forest.

3. HYDRODYNAMICAL SIMULATIONS

To understand pressure smoothing in the IGM we run high resolution cosmological hydrodynamical simulations using the energy- and entropy-conserving TreePM smoothed particle hydrodynamical (SPH) code P-GADGET-3, which is an updated version of the GADGET code (Springel et al. 2001; Springel 2005). In addition to the cosmological evolution of baryons and dark matter, this code implements photoionization and photoheating of baryons by calculating the equilibrium ionization balance of hydrogen and helium in a optically thin UV background, which is taken from an updated version of the model of Haardt & Madau (1996) presented by Davé et al. (1999). Radiative cooling is implemented by taking into account cooling via two-body processes such as collisional excitation of H I and He II, collisional ionization of H I, He I, and He II, recombination, and Bremsstrahlung (Katz et al. 1996). Likewise, P-GADGET-3 also includes inverse Compton cooling off the CMB (Ikeuchi & Ostriker 1986), which can be an important source of cooling at high redshifts. For temperatures in the range 10^4 – 10^5 K, at redshifts probed by the Ly α forest, recombination cooling is the dominant cooling mechanism (we ignore metal enrichment and its effect on cooling rates, which is a good approximation for the IGM).

Baryons with overdensities higher than a few hundred times the background density are expected to form galax-

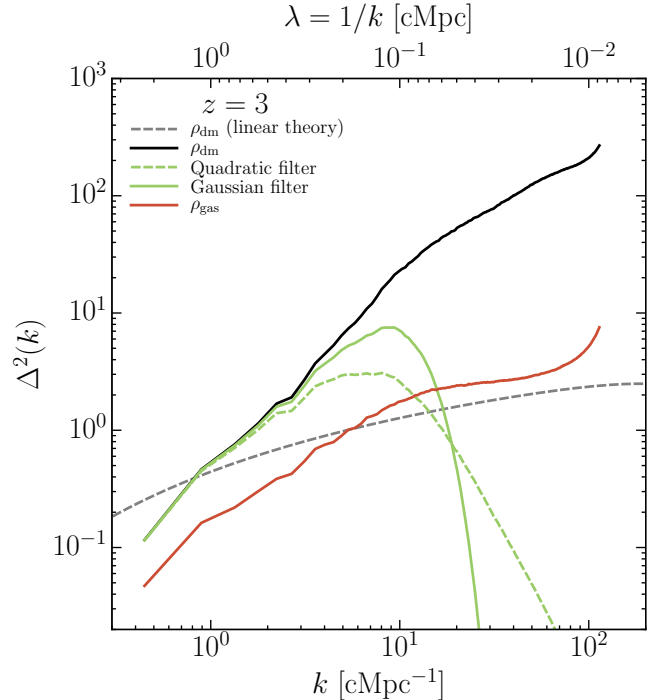


Figure 3. Gas (red curve) and dark matter (black curve) density power spectra at $z = 3$ in our fiducial simulation. Also shown are the linearly extrapolated matter power spectrum (dashed grey curve), and the quadratic (dashed green curve) and Gaussian (solid green curve) filters from Equations (5) and (9). The gas density power spectrum does not show a cut-off.

ies. But as these high density regions are not the subject of our study, we simplify their treatment. In the simulations presented here, all gas particles with temperature less than 10^5 K and overdensity of more than a thousand times the mean baryon density are converted to collisionless stars and removed from the hydrodynamical calculation (Viel et al. 2004). This speeds up the simulations, while leaving the low-density IGM unaffected. We use the QUICK_LYALPHA flag in P-GADGET-3 for this purpose, and in what follows we will also vary the value of this threshold to understand its impact on our results.

Simulations presented in this paper were all done in a cubic box of length 10 comoving h^{-1} Mpc on the side. Periodic boundary conditions were imposed. The number of dark matter and gas elements are both initially 512^3 . This corresponds to a dark matter particle mass of $M_{\text{dm}} = 4.5 \times 10^5 h^{-1} M_{\odot}$ and gas particle mass of $M_{\text{gas}} = 9.3 \times 10^4 h^{-1} M_{\odot}$. This gives us a mean inter-particle separation of better than 20 comoving h^{-1} kpc, which sets our spatial resolution in the lowest density regions of the IGM. This resolution is sufficient for simulating the Ly α forest (Bolton & Becker 2009; Lukić et al. 2015). Specifically, at $z = 2$ it has been found that a mass resolution of $M_{\text{gas}} = 1.6 \times 10^6 h^{-1} M_{\odot}$ is sufficient for convergence in the mean Ly α flux and flux power spectrum in GADGET (Bolton & Becker 2009). At higher redshifts, the mass resolution requirement grows stronger: at $z = 5$ a mass resolution of about $M_{\text{gas}} = 2 \times 10^5 h^{-1} M_{\odot}$ is required. Our mass resolution meets both these requirements (see also Bryan et al. 1999). However, in their study Bolton & Becker (2009) also found

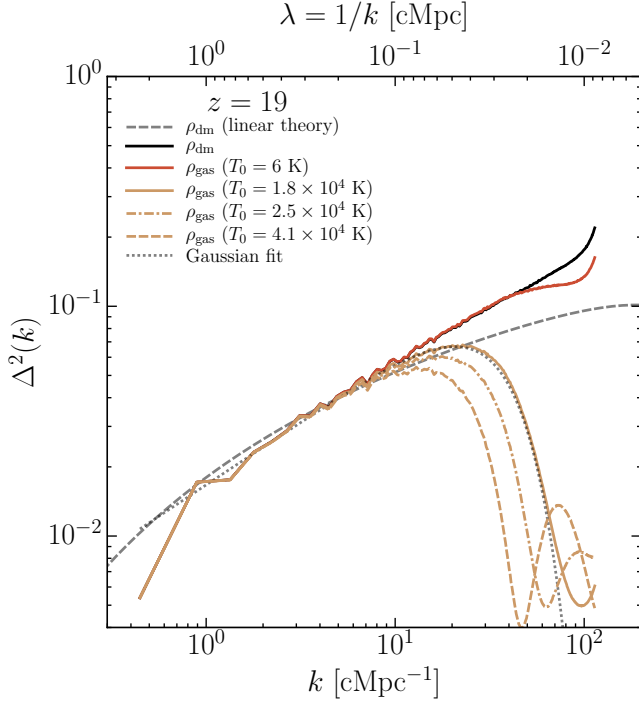


Figure 4. Gas density power spectrum at $z = 19$. The solid red curve shows the power spectrum in our fiducial run; solid, dashed, and dot-dashed beige curves show power spectra in simulations with high T_0 at this redshift. The dotted curve is a Gaussian fit to one of the power spectra. Also shown are the linear and nonlinear dark matter power spectra. In contrast to Figure 3, the gas power spectrum shows a Gaussian cut-off in accordance with Equation (9) at this high redshift when most scales in the box are linear. Note that in the fiducial simulation the pressure smoothing scale is too low to be resolved due to the low temperature at this high redshift.

that a box size of 10 comoving $h^{-1}\text{Mpc}$ is too small for convergence in these quantities, giving errors of about 10% for the flux power spectrum (see also Lukić et al. 2015). They find that a box size of at least 20 comoving $h^{-1}\text{Mpc}$ was required at $z = 2$. At $z = 5$, a box of size 40 comoving $h^{-1}\text{Mpc}$ was required. When the box size is small, the error due to the missing large-scale modes and the coupling of density perturbation modes in the box to modes larger than the box size is large. This results in the loss of the overall amplitude of the power spectrum of density perturbations (see also Meiksin & White 2004; McDonald et al. 2005; Viel & Haehnelt 2006; Tytler et al. 2009; Lidz et al. 2010; Lukić et al. 2015). However, as we will see below, this overall loss of power is not a concern for the purpose of characterizing the pressure smoothing scale.

Figure 1 shows distributions of gas and dark matter density from the fiducial simulation at $z = 3$ in slices approximately 20 comoving kpc/h thick. Gas and dark matter distributions are similar on large scales. But on small scales, the gas distribution is more diffuse. This difference is more prominent in quasi-linear structure such as filaments and is due to the pressure smoothing that we aim to characterize in this paper.

Apart from the fiducial simulation, we also present results from four other simulations, which differ from the fiducial simulation only in their thermal evolution. In these simulations, the photoheating rate of the H I, He I,

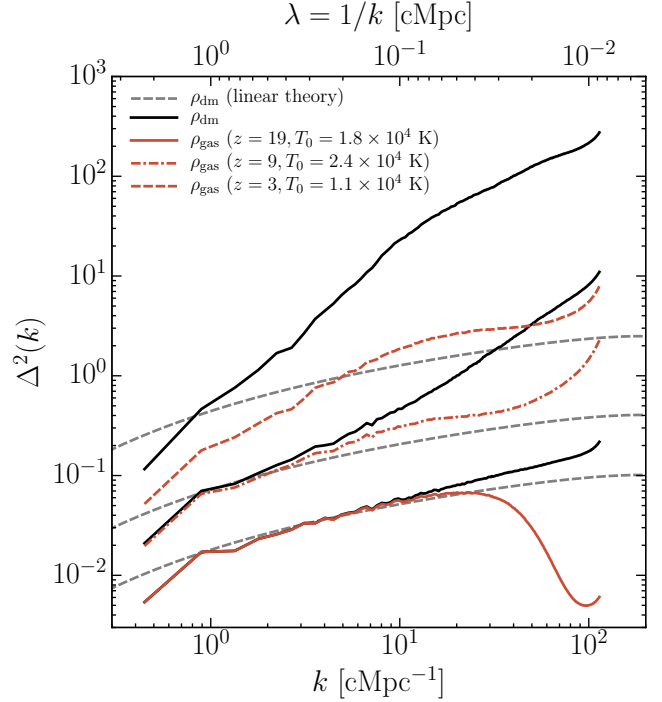


Figure 5. Evolution of the gas density power spectrum (red curves) from redshift 19 to 3 in a simulation in which the photoheating rate is enhanced so that the gas temperature is $T_0 \sim 10^4$ K at $z = 19$. Also shown are the nonlinear (solid black curves) and linear (dashed grey curves) dark matter density power spectra at each redshift. The gas power spectrum shows a Gaussian cut-off as expected from Equation (9) at $z = 19$, but this cut-off vanishes at low redshifts.

and He II in the IGM is enhanced artificially by constant factors of 2, 5, 10, and 50 (Becker et al. 2011) resulting in different thermal histories. The temperature of the IGM at mean density, T_0 at $z = 3$ for these simulations is, 1.4×10^4 K, 2.4×10^4 K, 3.6×10^4 K, and 8.6×10^4 K respectively. In the fiducial simulation T_0 at this redshift is 9.5×10^3 K. Figure 2 shows the phase space distribution of gas particles at $z = 3$ in the fiducial simulation and in the high-temperature simulation with $T_0 = 8.6 \times 10^4$ K. (Photoheating rate in this simulation is enhanced by a factor of 50 relative to the fiducial rate.) Both distributions have familiar features: an overwhelming fraction of low density ($\Delta < 10$) gas particles reside on the power law temperature-density relationship of the form given by Equation (1) shown by the dashed line. A fraction of the highest density gas ($\Delta > 100$) has cooled in collapsed haloes, and the rest is shock heated to virial temperatures exceeding 10^6 K. At this high redshift ($z = 3$) the low-density high-temperature warm hot intergalactic medium (WHIM; Cen & Ostriker 1999, 2006; Davé et al. 2001) is still sparsely populated. The phase space diagrams in Figure 2 show a cut-off at $\Delta = 10^3$ for temperatures below 10^5 K, which is due to the simple star formation recipe described above, which converts these cool high-density gas particles to stars.

For all simulations, we take snapshots of particle positions, velocity, temperature, and other properties. To calculate power spectra, we grid the relevant particles to create a density field, using a cloud-in-cell (CIC) scheme, taking into account the smoothing lengths of SPH par-

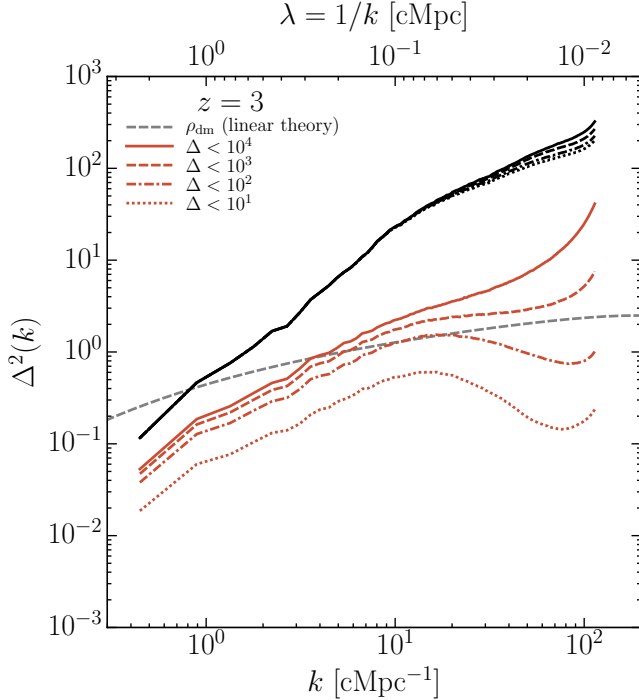


Figure 6. Gas density power spectrum with different star formation thresholds. The solid, dashed, dot-dashed, and dotted red curves show the gas density power spectra when the star formation threshold is set to 10^4 , 10^3 , 10^2 and 10 , respectively. The black curves show corresponding dark matter power spectra. Increasing the star formation threshold removes high density gas, which reduces small scale power.

ticles. After calculating the power spectrum, we deconvolve the CIC kernel, ignoring small errors due to aliasing on the smallest scales (Cui et al. 2008).

Ly α forest spectra are created from the particle distributions of each snapshot, accounting for the redshift-space distortions caused by peculiar velocities and thermal broadening. These are computed by accounting for the contributions to density, temperature and velocity of SPH particles closer to the sightline than their smoothing length, Doppler shifts due to the bulk velocity, and the thermal broadening of the Ly α absorption line. This procedure results in the Ly α flux as a function of wavelength or equivalently time or distance. Following the standard approach, we then rescale the UV background intensity so that the mean flux of these extracted spectra matches the observed mean flux at the respective redshift (Peeples et al. 2010a). We use the Ly α flux measurements reported by Faucher-Giguère et al. (2008) for this purpose.

4. CHARACTERIZING THE PRESSURE SMOOTHING SCALE

We now turn to the results of our simulations. Our first goal is to compare the simulations with the linear theory predictions of Equations (5) and (9).

4.1. Absence of a Cut-Off in the Gas Density Power Spectrum

Figure 3 shows the dimensionless power spectra of gas and dark matter density contrasts ($\delta = \rho/\bar{\rho} - 1$; for gas we use $\bar{\rho} = \Omega_b \rho_{\text{cr}}$) at $z = 3$ from our fiducial simulation. The

dark matter density power spectrum increases steeply towards small scales. The amplitude of the gas density power spectrum is suppressed relative to the dark matter at all scales probed by the simulation. Note that the enhancement in the dark matter power relative to the linear theory prediction indicates that scales of several Mpc are already nonlinear at this redshift. Therefore, it is clear that the pressure smoothing scale, which is expected to be of order 100 kpc, is already evolving non-linearly.

However, it is striking that in Figure 3 the gas density power does not exhibit a cut-off on any scale. This is very different from the linear theory expectations discussed in Section 2, which suggested a quadratic or Gaussian cut-off in the gas power spectrum at the pressure smoothing scale according to Equations (5) and (9). This discrepancy is highlighted in Figure 3, where the predictions of Equations (5) and (9) are also shown for an arbitrarily chosen pressure smoothing scale. The absence of a cut-off in the gas power spectrum shows that the linear theory formalism of Section 2 does not describe the physics of pressure smoothing on non-linear scales at $z = 3$. We observe similar behavior, i.e., an absence of a cut-off in the gas density power spectrum, in our simulations over the complete redshift range probed by the Ly α forest ($z \sim 2-5$).

To understand this large difference between the gas density power spectrum of Figure 3 and the linear theory predictions of Equations (5) and (9), it is useful to consider the gas and dark matter density power spectra at redshifts where density perturbations are still linear. We therefore look at the power spectra at $z = 19$ in Figure 4. At this high redshift, density perturbations are linear at most scales resolved in our box as indicated by the agreement of the dark matter density power spectrum with that predicted by linear theory in Figure 4. Scales ~ 100 kpc comparable to the pressure smoothing scale are quasi-linear, and the assumptions behind Equation (9) are thus still valid. We would therefore expect the gas power spectrum to exhibit a Gaussian cut-off. However, we face a different problem here at $z = 19$, namely that the gas temperature in the fiducial simulation is $T_0 = 6$ K as reionization does not occur until $z = 6$. At this low temperature, the filtering scale (Equation (8)) is expected to be ~ 2 kpc from Equation (2), much smaller than the smallest scale resolved in the simulation. As a result, there is no clear evidence for a cut-off in the gas density power spectrum. Indeed, in Figure 4, the gas and dark matter power spectra from the fiducial simulation agree at almost all scales, verifying our expectation that at low temperatures the tiny filtering scale ~ 2 kpc implies that gas follows dark matter for all scales resolved by the simulation.

To remedy this, we consider three other simulations for which we artificially enhance the H I photoheating rate between $z \sim 6$ and 30. Specifically, at redshifts $z < 6$ the photoheating rate is equal to that in the fiducial simulation, but it is set to be much higher (10^{-22} – 10^{-24} erg/s) at $z > 6$. These simulations with enhanced heating at high redshift can be thought of as “early reionization” models. Due to this enhanced heating the gas temperature at $z = 19$ is $T_0 \sim 10^4$ K in these simulations, which increases the pressure smoothing scale of Equation (8) to be well above the spatial resolution of our simulation

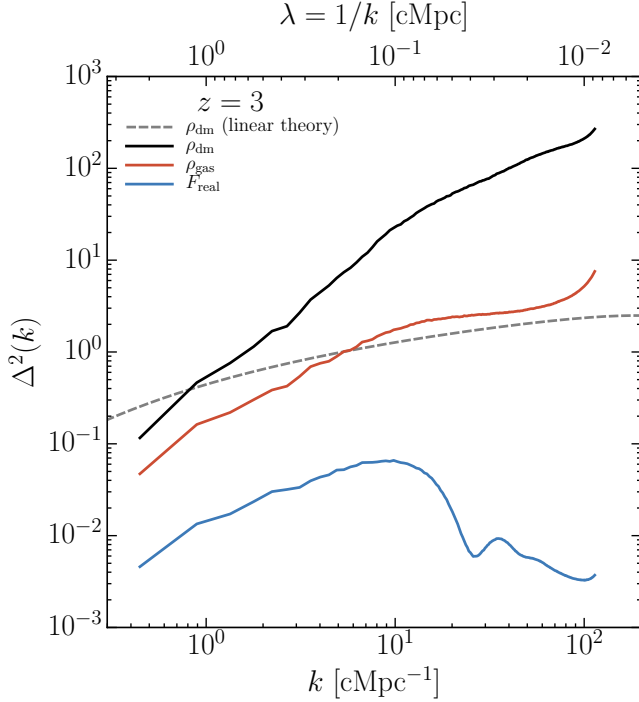


Figure 7. Power spectra of the dark matter density (black), gas density (red), and F_{real} (blue) fields at $z = 3$ from our fiducial simulation. The dashed grey curve shows the matter power spectrum prediction for linear growth of perturbations.

so that any cut-off will now be visible. Figure 4 shows the gas density power spectra at $z = 19$ from these three simulations with various enhanced heating rates and gas temperatures. The gas power is seen to drop precipitously between scales of 50 and 100 kpc, and the dotted curve shows that this cut-off has a Gaussian form, in accordance with Equation (9). Moreover, as the gas temperature T_0 increases, the cut-off is seen to move towards larger scales as expected for the pressure smoothing scale from Equation (8). Thus the classical pressure smoothing scale result appears to be valid at very high redshifts, when the ~ 100 kpc pressure smoothing scale is quasi-linear, but seems to break down at $z \sim 3$ when scales ~ 100 kpc become highly nonlinear.

This breakdown of the linear theory pressure smoothing scale picture is clearly indicated in Figure 5, which shows the evolution from $z = 19$ to 3 of gas and dark matter density power spectra in one of the simulations with enhanced photoheating at high redshifts. Comparison with the linear theory matter power spectrum (gray dashed curves) indicate that scales ~ 100 kpc are already highly nonlinear by $z = 9$. Hence one sees that at $z = 19$, when the pressure smoothing scale is quasi-linear, the gas power spectrum shows a clear Gaussian cut-off at 50 comoving kpc, whereas at lower redshifts when this scale is highly nonlinear this cut-off vanishes. In what follows, we will explain why the cut-off disappears at low redshifts and will present a method to reveal it.

4.2. The Role of High Density Gas

As we saw above in Figure 4, the gas density power spectrum does not exhibit any cut-off in power at scales ~ 100 kpc at relatively low redshifts ($z \sim 3$) in our fiducial

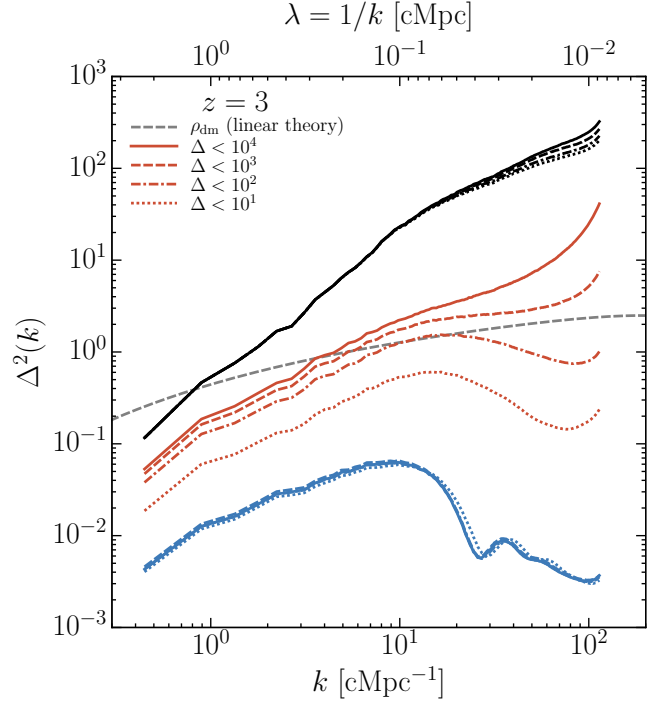


Figure 8. F_{real} power spectra with different star formation density thresholds. The threshold, which acts as a crude model of galaxy formation, affects the gas density power spectra dramatically but F_{real} is insensitive to it.

simulation. At these redshifts and small scales, the power is completely dominated by highly overdense and non-linear collapsed structures, namely halos. Although these structures occupy a tiny volume fraction, they nevertheless have a large impact on the power spectrum. Recall that galaxy formation is simplified in our fiducial simulation: all gas particles with overdensity greater than 10^3 and temperature less than 10^5 K are converted into stars. This results in a stellar density parameter $\Omega_* = 0.0075$ at $z = 3$, which is already factor of three higher than the measured value of $\Omega_* = 0.0027$ at $z = 0$ (Fukugita & Peebles 2004). We now rerun this simulation, with the same initial conditions, but with modified star-formation overdensity thresholds of 10^4 , 100, and 10. At $z = 3$ we find that thresholds of 10^4 , 10^3 , 100, and 10, result in $\Omega_* = 0.0066$, 0.0075, 0.0092, and 0.0145, respectively. As we reduce the star formation density threshold, we form more stars but at the same time we remove more high density gas from our simulation and the power spectrum analysis.

Figure 6 shows the resulting gas density power spectra for these different star-formation density thresholds. As the density threshold is progressively decreased, and more high density gas is removed from the simulation, we see that the power on scales smaller than $\lesssim 100$ kpc is increasingly attenuated, and the overall amplitude of the power on larger scales is also reduced. This behavior is not unexpected, and can be understood in a halo model picture (Cooray & Sheth 2002). As dense gas above the star-formation threshold is removed, we effectively mask dense gas in collapsed haloes in the simulation volume. The truncation of the small scale power arises from the removal of this gas, which can be thought of as sup-

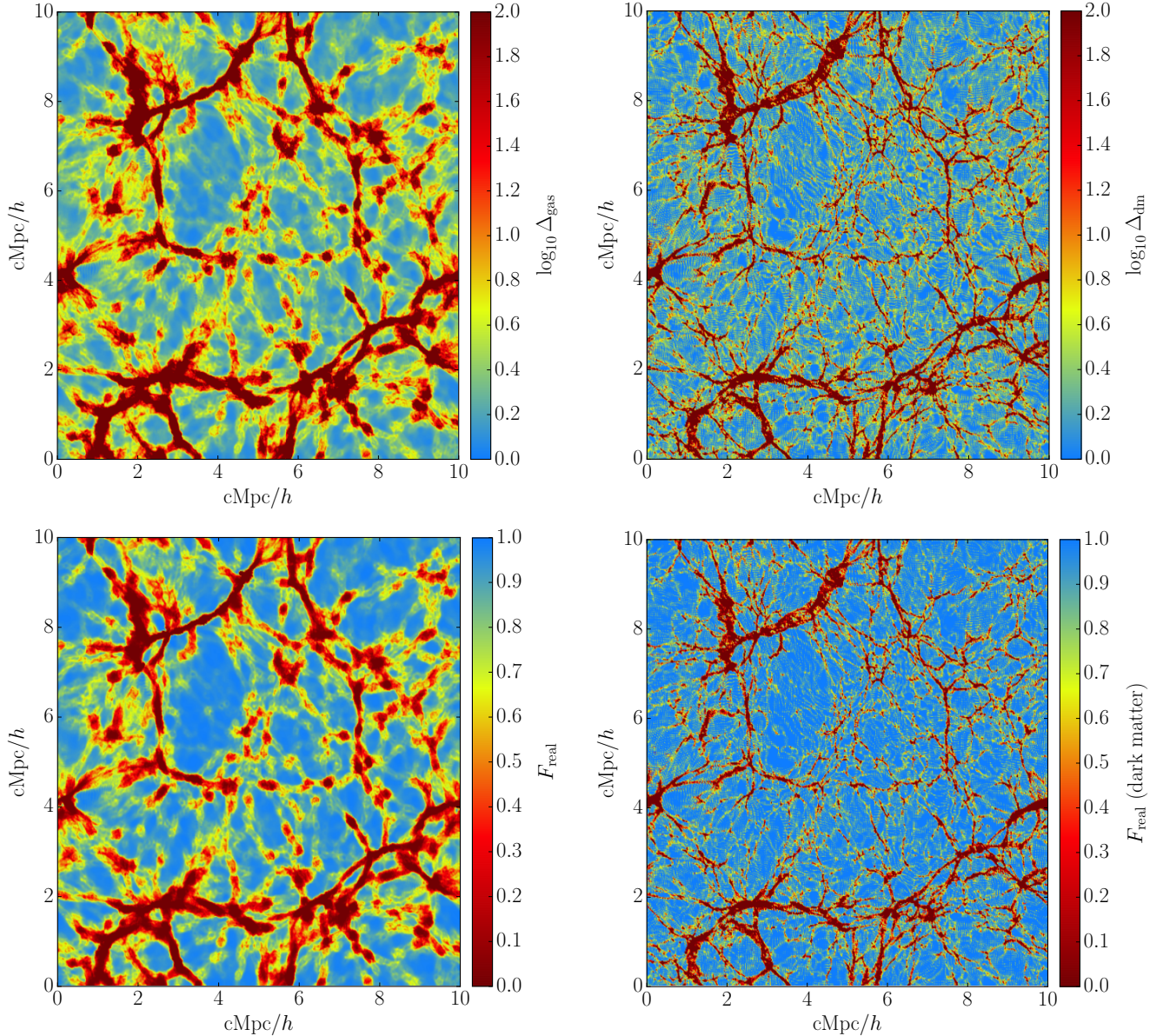


Figure 9. Slices of gas (top left) and dark matter (top right) density, and of the F_{real} distribution calculated from gas (bottom left) and dark matter (bottom right) distributions at $z = 3$ in our fiducial simulation. Density at each point is an average on a cubical cell approximately 20 kpc/h on a side. Each slice has a thickness of one cell length. Note that the color scale in panels showing F_{real} is inverted. The mapping from density to F_{real} reduces high density regions to zero.

pressing the ‘one-halo’ term of the gas power spectrum. However, part of the large scale power of the gas density also arises from the clustering of these halos, i.e. the ‘two halo term’, hence masking haloes results in a reduction of large scale power as well. Therefore on large scales, the net effect of the star-formation threshold is to introduce a linear bias, such that the power spectra for different star-formation thresholds in Figure 6 are all parallel to each other at small k values. Figure 6 thus shows us that the gas density power spectrum is indeed strongly influenced by nonlinear structure. More importantly, as the highest density regions are removed, the gas distribution begins to show a hint of a cut-off in power. This is seen most clearly in the $\Delta < 10$ curve in Figure 6.

In other words, to recover the signature of pressure

smoothing in the moderately overdense IGM ($\Delta \lesssim 10$), we need to remove the influence of gas in high-density regions, which would otherwise dominate the small-scale power. One way of doing this is by applying an ad hoc cut-off in gas density as done in Figure 6. However, the choice of this density threshold is arbitrary—it would need to be made redshift-dependent, as the amount of high-density gas that has collapsed to form stars increases at later times, and is thus dependent on the galaxy formation model in the simulation, which we have crudely parameterized here with a simple star-formation density threshold. However, even in more sophisticated simulations which attempt to model detailed baryonic process in galaxies such as star-formation and feedback using a combination of higher resolution and sub-grid

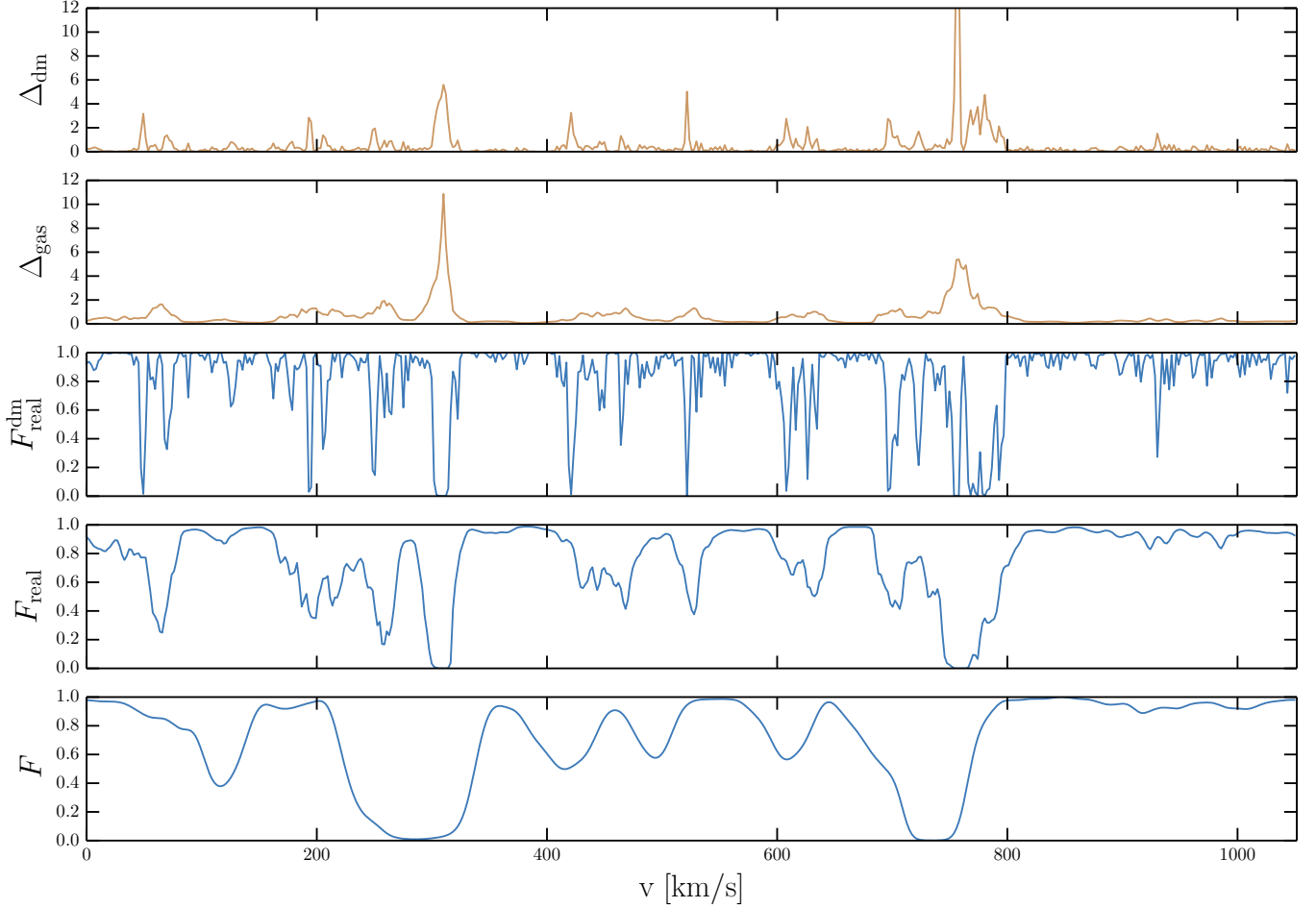


Figure 10. Distribution of various quantities along a randomly-chosen line of sight through our fiducial simulation. From top to bottom, panels show the dark matter overdensity, gas overdensity, the distribution of F_{real} calculated under the assumption that gas follows dark matter at all scales (see Section 4.4), and the distribution of F_{real} calculated from the gas distribution in the simulation. The bottom panel shows the Ly α flux along the line of sight, where the effect of longitudinal thermal line-broadening and redshift-space distortions are clearly seen.

modeling (e.g., Schaye et al. 2010; Vogelsberger et al. 2014; Crain et al. 2015), our findings indicate that the the small scale baryon power spectrum will be influenced by the details of galaxy formation and the specific subgrid implementation. Therefore the challenge is to devise a more robust method of removing the influence of high density gas on small scale power.

4.3. Real-Space Flux Reveals Pressure Smoothing in Baryons

In this section we introduce a better method for revealing the three-dimensional cut-off in the baryon power of the moderate overdensity IGM. Given the three-dimensional, statistically isotropic gas density field, we calculate the *real-space* Ly α flux at each point in the box. This quantity, which we denote by F_{real} , is defined by

$$F_{\text{real}} \equiv \exp(-\tau_{\text{real}}), \quad (10)$$

where the real-space Ly α absorption optical depth is given by

$$\tau_{\text{real}} = \frac{3\lambda_{\alpha}^3 \Lambda_{\alpha}}{8\pi H(z)} n_{\text{HI}}. \quad (11)$$

Here $\lambda_{\alpha} = 1216 \text{ \AA}$ is the rest-frame Ly α wavelength, Λ_{α} is the Einstein A coefficient (also written as A_{10} and can be written in terms of an oscillator strength), $H(z)$ is the Hubble constant, and n_{HI} is the number density of neutral hydrogen. The definition in Equation (11) is identical to the Gunn-Peterson formula used to compute the Ly α forest optical depth, except that the convolution integral which accounts for the redshift-space effects of the peculiar velocity field and thermal line broadening has not been included. Indeed, we have chosen to define a statistic in real space precisely because these redshift-space effects, specifically the line-of-sight smoothing due to thermal broadening, are in fact degenerate with the three-dimensional real-space Jeans smoothing that we aim to study. Hence, F_{real} is a three-dimensional, statistically isotropic field.

The neutral hydrogen density is given by

$$n_{\text{HI}} = \frac{\alpha_R(T) n_{\text{H}}^2}{\Gamma_{\text{HI}}}, \quad (12)$$

where $n_{\text{H}} = 0.76\rho_{\text{gas}}$ is the total hydrogen density, Γ_{HI} is the H I photoionization rate, $\alpha_R(T) \propto T^{-0.7}$ is the hydrogen recombination rate. Therefore, in a highly ion-

ized IGM where the gas lies on a well-defined temperature density relation $T \propto \rho^{\gamma-1}$ (see Figure 2), the neutral hydrogen number density and the optical depth in Equation (11) are proportional to a power of the total gas density $\rho^{2-0.7(\gamma-1)}$. (When all gas is assumed to lie on the temperature-density relation, Equation (12) constitutes the Fluctuating Gunn-Peterson Approximation (FGPA).) Thus, F_{real} is proportional to the *exponential* of this power of the gas density, and it exponentially suppresses the contribution of the high density regions. This is of course another way to say that the high density regions have large optical depth and therefore result in completely saturated Ly α absorption, i.e., have $F_{\text{real}} = 0$.

F_{real} is not a directly observable field, but it can nevertheless be constrained by close quasar pair observations (Rorai et al. 2013). The phase angle differences between homologous line-of-sight Fourier modes in quasar pair spectra can be written as

$$\theta_{12}(k) = \cos^{-1} \left[\frac{\text{Re}(F_{1k}^* F_{2k})}{|F_{1k} F_{2k}|} \right], \quad (13)$$

where $F_1(k)$ and $F_2(k)$ are Fourier amplitudes of the two quasars in a pair. Rorai et al. (2013) showed that the probability distribution of these phase differences $\theta_{12}(k)$ is sensitive to a smoothing cut-off in the underlying field. For modes with wavelength larger than the pair separation r_{\perp} , $k \ll k_{\perp} \sim 1/r_{\perp}$, the mean value of $\theta_{12}(k)$ can be written as (Rorai et al. 2013)

$$\langle \cos \theta(k, r_{\perp}) \rangle \approx \frac{\int_{k_{\perp}}^{k_{\parallel}} dk' k' J_0(r_{\perp} \sqrt{k'^2 - k^2}) P_{F_{\text{real}}}(k')}{\int_{k_{\perp}}^{\infty} dk' k' P_{F_{\text{real}}}(k')} \quad (14)$$

where J_0 is the Bessel function of zeroth order and $P_{F_{\text{real}}}$ is the three-dimensional power spectrum of F_{real} . Thus by measuring the phase angle probability distribution function in close quasar pairs the F_{real} can be directly constrained.

Note that in the construction of the F_{real} field using Equation 10, we use the rescaled photoionization rate Γ_{HI} that produces the correct observed mean *redshift-space* flux as discussed in Section 3 above. In this approach, we rescale the UV background intensity so that the mean redshift-space flux of these extracted spectra matches the observed mean redshift-space flux at the respective redshift (Faucher-Giguère et al. 2008). When this rescaled background is used in calculating the real-space flux F_{real} , its mean value is not exactly the same as the mean redshift-space flux, although the differences are very small. For instance, in our fiducial simulation, the mean redshift-space flux at $z = 3$ is 0.680 after rescaling the UV background, while the corresponding mean value of F_{real} , using this same background, is 0.679. Equations (11) and (12) indicate that rescaling the UV background to match the observed mean flux values is tantamount to fixing the range of gas densities probed by the flux field. As such, the very close agreement between the mean of the redshift space F and real-space F_{real} flux indicates that F_{real} and F probe nearly identical gas densities.

In Figure 7 we now look at the three-dimensional power spectrum of the distribution of F_{real} at $z = 3$ in our fiducial simulation (recall that unlike the observed Ly α flux, F_{real} is statistically isotropic). Figure 7 also shows the

gas and dark matter density power spectra for comparison. The most conspicuous feature of the F_{real} power spectrum in Figure 7 is that it exhibits a small-scale cut off, located at around $k = 20 \text{ h/Mpc}$ (about $\lambda = 35$ comoving kpc)⁸. This is reminiscent of the Gaussian filtering scale cut-off that we expect from linear theory. There is also an overall reduction in the amplitude of the F_{real} power relative to that of the gas density. This reduced power level is similar to that seen when we applied a star formation density threshold in Figure 6, and, which we argued can also be understood in the halo model picture. Generically, a nonlinear transformation of the density field, such as F_{real} , will have a power spectrum that has a different shape than that of the density, but for small k where the Fourier amplitudes are small, the transformation can be linearized such that the power will appear to be a linear bias rescaling of that of the original density field.

Thus F_{real} provides a natural way of removing the influence of high density regions in our analysis, and reveals the small-scale structure of the IGM—in the form of a sharp cut-off in the power at a certain scale—that is presumably due to pressure smoothing. Furthermore, this definition of F_{real} is robust against arbitrary choices of galaxy formation prescriptions in our simulations. Recall that, as discussed in Section 4.2, we can think of variation in the star formation threshold as variation in our (crude) galaxy formation prescriptions. The red curves in Figure 8 illustrate that the gas density power spectrum varies dramatically as the star formation density thresholds is varied from 10^4 to 10. As the threshold is decreased, power at small scales is considerably reduced, but a clear signature of the pressure smoothing is not apparent from these curves. The removal of clustered high-density regions, also reduces the large-scale power as a linear-bias rescaling. Although the density power varies dramatically depending on the details of how galaxy formation is treated, the blue curves in Figure 8 show that the shape of the F_{real} power spectrum is invariant to these changes. Thus the F_{real} field as defined in Equation (10) provides an unambiguous way of characterizing the cut-off, valid at all relevant redshifts regardless of the galaxy formation details used in the simulation.

4.4. Visualizing the F_{real} Field

Figure 9 shows a slice of the F_{real} field at $z = 3$ from our fiducial simulation in comparison with a slice of the gas density field. There is an almost one-to-one correspondence between gas density and F_{real} . This correspondence results from ignoring redshift-space distortions due to peculiar velocities and thermal broadening. The value of F_{real} is highest (~ 1) in regions with lowest gas density, whereas all high density filaments and haloes are mapped to $F_{\text{real}} = 0$. This is exactly the kind of suppression of high densities required to reveal the structure of the low-density IGM. Note that unlike in Figure 1, we have chosen a linear color scale in the gas density plot to highlight the saturation of F_{real} values at high densities.

For the sake of illustration, we also apply the transform

⁸ Note that we choose to define the upper-axis as $1/k$ instead of $2\pi/k$ because for a Gaussian smoothing the Fourier space cut off is inverse of that in the real space. As we see below, the cut off in F_{real} has a Gaussian form.

mation encoded in F_{real} on the dark matter density field. This should be understood as the F_{real} field in the limit where the baryons directly trace the dark matter density, but nevertheless adhere to the nonlinear transformation in Equation (12). This is achieved by “gassifying” dark matter, i.e., mapping the dark matter density field to a pseudo-gas density field through

$$\rho_{\text{gas}} = \rho_{\text{dm}} \left(\frac{\Omega_b}{\Omega_m - \Omega_b} \right), \quad (15)$$

which traces the dark matter at all scales. In other words, as the dark matter is cold and pressureless and exhibits significant small-scale power, this pseudo-gas distribution has no pressure smoothing scale.

The neutral hydrogen number density, n_{HI} , is then calculated by imposing the same temperature-density relation on these pseudo-gas particles as our fiducial simulation, i.e., by using FGPA. A slice of the resulting $F_{\text{real}}^{\text{dm}}$ field calculated in this fashion is shown in the lower right panel of Figure 9. Its structure is markedly different from that of the F_{real} field calculated from the gas distribution. The $F_{\text{real}}^{\text{dm}}$ has a morphology very similar to the dark matter density distribution, and because it lacks a pressure smoothing scale cut-off, has a significant amount of small-scale structure. In contrast the pressure smoothing of the gas distribution makes the F_{real} field smoother and more diffuse. Although somewhat contrived, $F_{\text{real}}^{\text{dm}}$ is helpful in better understanding the F_{real} transformation of the density field.

These points are further illustrated in Figure 10, which compares the F_{real} field along an example line of sight through our fiducial simulation to various other quantities at $z = 3$. The upper two panels of this figure show the dark matter and gas density field along the line of sight. As in Figure 9, we see that the gas density field is a smoothed version of the dark matter density field. The third and fourth panels of Figure 10 show the $F_{\text{real}}^{\text{dm}}$ and F_{real} fields, calculated from the dark matter and gas density fields respectively. The mapping to real space flux makes the smoothness of the gas density field relative to the dark matter density field much more apparent. The last panel shows the observed, redshift-space Ly α flux, F , which includes the effects of peculiar velocities and thermal broadening. As a result, the absorption features in F are shifted because of peculiar velocities, and their widths now reflect the impact of Hubble flow and are much smoother because of thermal line broadening. The comparison between F_{real} and F is striking, and illustrates that the intrinsic small-scale structure of the gas in real space, which is determined by pressure smoothing, is completely hidden by redshift space effects.

Finally, it is instructive to examine the power spectrum of the $F_{\text{real}}^{\text{dm}}$ field, which is shown as a dashed curve in Figure 11. As expected, the power spectrum of $F_{\text{real}}^{\text{dm}}$ shows no evidence for a small-scale cut-off: because the dark matter is not smoothed by pressure there is power on arbitrarily small scales. The power spectrum at large scales is parallel to that for F_{real} obtained from the gas distribution but the amplitude is lower.⁹ This comparison demonstrates that the cut-off in the power spectrum

⁹ The F_{real} and $F_{\text{real}}^{\text{dm}}$ fields are non-linear transformations of the gas and dark matter density fields respectively. Expressing the power spectrum of these non-linear quantities in terms of the origi-

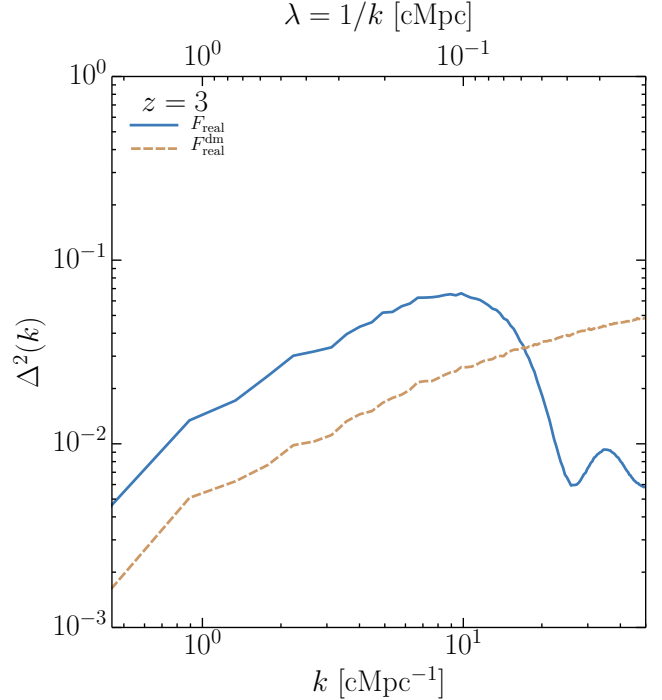


Figure 11. Power spectrum of the F_{real} distribution when calculated under the assumption that gas follows dark matter at all scales (dashed curve), compared to the power spectrum of F_{real} calculated from the actual gas distribution in the simulation (solid curve).

of the F_{real} distribution in our simulations results from pressure smoothing.

4.5. Quantifying the pressure smoothing scale

We have demonstrated that the power spectrum of the F_{real} field shows a conspicuous small-scale cut-off, which we have interpreted as an effect of pressure smoothing. In this section we quantify the location of this cut-off, and demonstrate that its location behaves as expected from the classical Jeans scale argument.

Inspection of the F_{real} power spectrum in Figure 7 motivates a simple fitting function of a power law power spectrum cut off by a Gaussian:

$$\Delta_F^2(k) = Ak^n \exp\left(-\frac{k^2}{k_{\text{ps}}^2}\right), \quad (16)$$

which has three parameters: A , n , and k_{ps} . Figure 12 shows that Equation (16) is an excellent fit to the power spectra of F_{real} in our simulations. The fitting function

nal field requires computing a complicated mode-coupling integral, which couples large and small scale power. As such the reduced amplitude of $F_{\text{real}}^{\text{dm}}$ relative to F_{real} is related to the different shapes of the gas and dark matter power spectra. The reduced amplitude of $F_{\text{real}}^{\text{dm}}$ is intuitive when one realizes that both F_{real} and $F_{\text{real}}^{\text{dm}}$ span the same domain from zero to unity and have nearly identical mean values, whereas the variance of $F_{\text{real}}^{\text{dm}}$ is comparable to that of F_{real} (although slightly higher because of additional small-scale power). The variance of a field is $\sigma^2 = 1/2\pi \int \Delta^2(k) d \log k$, which is proportional to the area under the curves in Figure 11. Thus given the extra small-scale power in $F_{\text{real}}^{\text{dm}}$, in order for $F_{\text{real}}^{\text{dm}}$ and F_{real} to have comparable variance, the overall amplitude of $F_{\text{real}}^{\text{dm}}$ must be lower.

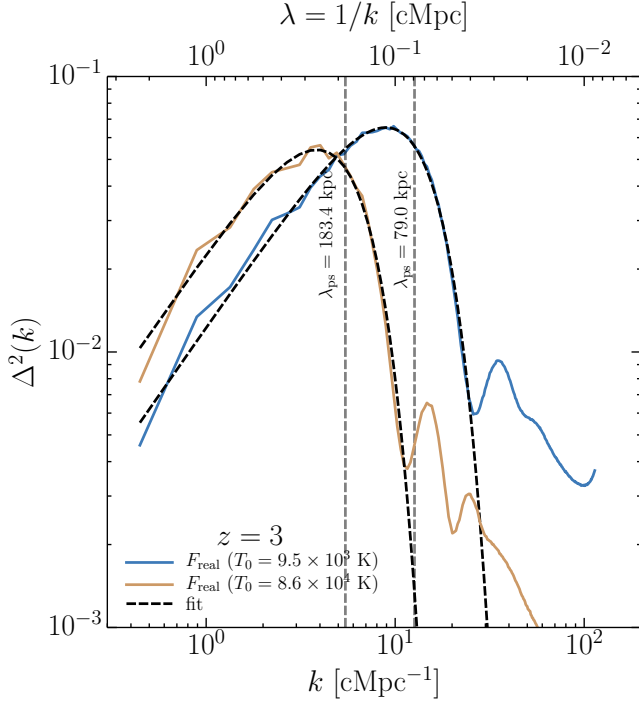


Figure 12. Fits to F_{real} power spectra from two simulations with different temperatures showing that the cut-off in the power spectrum is Gaussian. Blue and beige curves show the F_{real} power spectra from the simulations; black dashed curves are fits. The effect of temperature on the cut-off is evident.

allows us to quantify the pressure smoothing scale in our fiducial simulation ($T_0 = 9.5 \times 10^3$ K) as $\lambda_{\text{ps}} = 1/k_{\text{ps}} = 79.0$ comoving kpc at $z = 3$. In the simulation in which the temperature at the mean density of the IGM, $T_0 = 8.6 \times 10^4$ K, is higher than that in the fiducial simulation by a factor of ~ 10 , is $\lambda_{\text{ps}} = 191.5$ comoving kpc.

In Figure 13, we compare the F_{real} power spectra in five simulations with different temperatures ranging from $T \sim 10^4$ to $\sim 10^5$. As expected, the dark matter density power spectra are essentially identical for all temperatures. The gas density power spectrum shows some change due to the change in temperature, but these small differences would be masked if galaxy formation were treated differently (see Figure 6), as we argued in Section 4.2. Much more significant changes are seen in the F_{real} power spectrum, where the cut-off scale is observed to progressively increase with temperature. Thus F_{real} successfully captures a temperature-dependent smoothing of the gas density field.

The temperature dependence of the pressure smoothing scale $\lambda_{\text{ps}} \equiv 1/k_{\text{ps}}$ as determined by fitting Equation (16) to the F_{real} power spectrum of simulations with varying gas temperature is shown in Figure 14. The blue and brown curves show the temperature dependence of the linear theory Jeans scale, $\lambda_J \propto \sqrt{T_0}$, and the linear theory filtering scale, λ_F , defined in Equations (2) and (8), respectively. Both of these quantities were derived by measuring the thermal evolution of gas in the simulations. As expected at this post-reionization redshift ($z = 3$), the filtering scale is smaller than the Jeans scale, by a factor of ~ 3 in this case (Gnedin & Hui 1998; Gnedin et al. 2003). We see that the tempera-

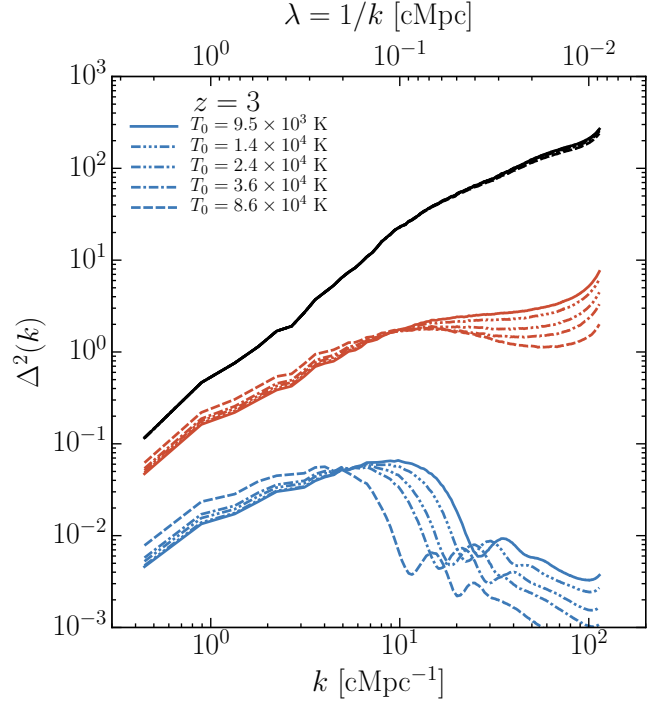


Figure 13. Power spectra of the dark matter density, gas density, and F_{real} fields at $z = 3$ in our five simulations with different thermal histories. The dark matter density power spectra are identical for all temperatures. The gas density power spectrum shows some change due to the change in temperature, but these small differences would change if galaxy formation were treated differently. Much more significant changes are seen in the F_{real} power spectrum, where the cut-off scale is observed to progressively increase with temperature.

ture dependence of the pressure smoothing scale defined by our fitting function in Equation (16) is nearly identical to the $\sqrt{T_0}$ dependence of the linear theory Jeans and filtering scales, which clearly demonstrates that it is probing pressure support in the IGM. Note that the slight deviation of our λ_{ps} values from the exact \sqrt{T} dependence is partly due to the fact that simulations with different temperatures actually probe somewhat different gas densities. This occurs because we always rescale the UV background of these simulations to have the same observed mean flux value, and by changing the UV background, one changes the mapping between flux and density, and hence the range of densities probed by each model. This also explains why the pressure smoothing scale is higher than the filtering scale, as the former probes pressure smoothing at higher densities than the mean density and therefore at higher temperatures than T_0 (Schaye 2001).

This simple fitting function for F_{real} in Equation (16) now allows us to quantify the pressure smoothing of the IGM, and make meaningful statements about the pressure smoothing scale for any thermal model and reionization history.

5. CONCLUSIONS

In this paper, we presented high-resolution hydrodynamical simulations and provided a method to characterize the pressure smoothing scale of the IGM. We propose a new statistic, which we call the real-space flux,

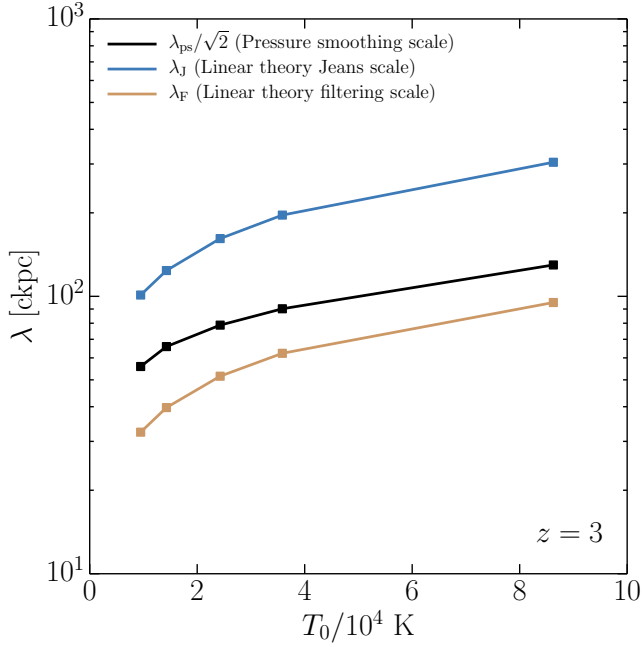


Figure 14. Temperature dependence of the pressure smoothing scale at $z = 3$ (black curve) in five of our simulations with different values of T_0 . The pressure smoothing scale increases with increasing T_0 . The blue and brown curves show the temperature dependence of the linear theory Jeans scale, $\lambda_J \propto \sqrt{T_0}$, and the linear theory filtering scale, λ_F , defined in Equations (2) and (8), respectively. The temperature dependence of the pressure smoothing scale is nearly identical to the $\sqrt{T_0}$ dependence of the linear theory Jeans and filtering scales. (The pressure smoothing scale is defined by fitting the form in Equation (16) to the flux power spectrum, whereas the other two scales in this figure are defined in terms of density contrasts. Therefore, for consistency, the pressure smoothing scale has been divided by $\sqrt{2}$.)

F_{real} , which is related to observations of correlated Ly α forest absorption in close quasar pairs and is key to their interpretation. Our chief conclusions are:

- The structure of the IGM in hydrodynamical simulations is very different from linear theory expectations at redshifts probed by the Ly α forest. The gas density power spectrum does not exhibit any apparent small-scale cut-off, which is the expected signature of pressure smoothing in the IGM.
- This expected cut-off in the gas power spectrum is buried under the contribution of dense gas in collapsed halos, which dominates the small-scale power. As this dense gas is governed by the highly uncertain physics of galaxy formation and the circumgalactic medium, disentangling the high and low density regions of the baryonic field is crucial to reveal pressure smoothing.
- We have introduced a new field, the real-space Ly α flux, F_{real} , which naturally suppresses high density regions associated with galactic halos, and provides an unambiguous characterization of pressure smoothing in the IGM. The power spectrum of F_{real} cuts off at a well-defined scale, which depends on gas temperature as expected for the classical Jeans scale, making F_{real} an effective tool for studying IGM pressure smoothing.

- We provide a fitting function that accurately describes the power spectrum of F_{real} , and defines the pressure smoothing scale as the small-scale cut-off of the F_{real} power. This characterization of pressure smoothing enables one to measure the IGM pressure smoothing scale from any hydrodynamical simulation, and thus ask meaningful questions about its dependence on the thermal and reionization history. Furthermore, it is directly related to observational measurements of correlated Ly α forest absorption in close quasar pair spectra.

Whereas to date, studies of the thermal state of the IGM have focused largely on the amplitude T_0 and slope γ of the temperature-density relation at a given redshift z , the results of this paper enable one to augment this standard description of the IGM with a third parameter λ_{ps} that describes the pressure smoothing scale, which depends on the full thermal and reionization history. This characterization of the pressure smoothing scale is crucial for interpreting current measurements of the thermal state of the IGM from line-of-sight observations of the Ly α forest, and is also critical for interpreting measurements of the pressure smoothing scale from quasar pair observations.

Indeed, measurements of the pressure smoothing scale using close quasar pairs hold tremendous promise (Rorai et al. 2013, Rorai et al. in prep.). The sensitivity of the pressure smoothing scale to the thermal and reionization history of the IGM will be discussed in an upcoming paper (Oñorbe et al. in prep.). We will also study the requirements for resolving the pressure smoothing scale in hydrodynamical simulations, and the convergence criteria for simulating a grid of IGM models with different thermal histories (Oñorbe et al. in prep.). Measurements of the pressure smoothing scale and comparison to these types of theoretical modeling provides a new window for understanding the small-scale structure and thermal and reionization history of the IGM. The F_{real} statistic introduced in this paper provides an important new technique for relating simulations of the low-density IGM to this new observable.

ACKNOWLEDGMENTS

We acknowledge helpful comments from the referee, Nick Gnedin, and useful discussions with Martin Haehnelt, Nishikanta Khandai, Zarija Lukić, Peter Nugent, Ewald Puchwein, Casey Stark, Greg Stinson, and Martin White. JFH acknowledges generous support from the Alexander von Humboldt foundation in the context of the Sofja Kovalevskaja Award. The Humboldt foundation is funded by the German Federal Ministry for Education and Research.

REFERENCES

- Barkana, R., & Loeb, A. 2001, Phys. Rep., 349, 125
- Becker, G. D., Bolton, J. S., Haehnelt, M. G., & Sargent, W. L. W. 2011, MNRAS, 410, 1096
- Bi, H., & Davidsen, A. F. 1997, ApJ, 479, 523
- Bi, H. G., Boerner, G., & Chu, Y. 1992, A&A, 266, 1
- Binney, J., & Tremaine, S. 2008, Galactic Dynamics: Second Edition (Princeton University Press)
- Boera, E., Murphy, M. T., Becker, G. D., & Bolton, J. S. 2014, MNRAS, 441, 1916
- Bolton, J. S., & Becker, G. D. 2009, MNRAS, 398, L26

- Bolton, J. S., Becker, G. D., Haehnelt, M. G., & Viel, M. 2014, *MNRAS*, 438, 2499
- Bolton, J. S., Becker, G. D., Raskutti, S., Wyithe, J. S. B., Haehnelt, M. G., & Sargent, W. L. W. 2012, *MNRAS*, 419, 2880
- Bolton, J. S., Becker, G. D., Wyithe, J. S. B., Haehnelt, M. G., & Sargent, W. L. W. 2010, *MNRAS*, 406, 612
- Bolton, J. S., Viel, M., Kim, T.-S., Haehnelt, M. G., & Carswell, R. F. 2008, *MNRAS*, 386, 1131
- Bryan, G. L., Machacek, M., Anninos, P., & Norman, M. L. 1999, *ApJ*, 517, 13
- Bryan, G. L., & Machacek, M. E. 2000, *ApJ*, 534, 57
- Calura, F., Tescari, E., D’Odorico, V., Viel, M., Cristiani, S., Kim, T.-S., & Bolton, J. S. 2012, *MNRAS*, 422, 3019
- Cen, R., Miralda-Escudé, J., Ostriker, J. P., & Rauch, M. 1994, *ApJ*, 437, L9
- Cen, R., & Ostriker, J. P. 1999, *ApJ*, 514, 1
- . 2006, *ApJ*, 650, 560
- Chang, P., Broderick, A. E., & Pfrommer, C. 2012, *ApJ*, 752, 23
- Choudhury, T. R., Padmanabhan, T., & Srianand, R. 2001a, *MNRAS*, 322, 561
- Choudhury, T. R., Srianand, R., & Padmanabhan, T. 2001b, *ApJ*, 559, 29
- Cooray, A., & Sheth, R. 2002, *Phys. Rep.*, 372, 1
- Crain, R. A., et al. 2015, arXiv:1501.01311 [astro-ph.GA]
- Croft, R. A. C., Hernquist, L., Springel, V., Westover, M., & White, M. 2002, *ApJ*, 580, 634
- Croft, R. A. C., Weinberg, D. H., Katz, N., & Hernquist, L. 1998, *ApJ*, 495, 44
- Cui, W., Liu, L., Yang, X., Wang, Y., Feng, L., & Springel, V. 2008, *ApJ*, 687, 738
- Davé, R., Hernquist, L., Katz, N., & Weinberg, D. H. 1999, *ApJ*, 511, 521
- Davé, R., et al. 2001, *ApJ*, 552, 473
- Faucher-Giguère, C.-A., Lidz, A., Hernquist, L., & Zaldarriaga, M. 2008, *ApJ*, 688, 85
- Fukugita, M., & Peebles, P. J. E. 2004, *ApJ*, 616, 643
- Garzilli, A., Bolton, J. S., Kim, T.-S., Leach, S., & Viel, M. 2012, *MNRAS*, 424, 1723
- Garzilli, A., Theuns, T., & Schaye, J. 2015, arXiv:1502.05715 [astro-ph.CO]
- Gnedin, N. Y., & Hui, L. 1998, *MNRAS*, 296, 44
- Gnedin, N. Y., et al. 2003, *ApJ*, 583, 525
- Haardt, F., & Madau, P. 1996, *ApJ*, 461, 20
- Haehnelt, M. G., & Steinmetz, M. 1998, *MNRAS*, 298, L21
- Hernquist, L., Katz, N., Weinberg, D. H., & Miralda-Escudé, J. 1996, *ApJ*, 457, L51
- Hinshaw, G., et al. 2013, *ApJS*, 208, 19
- Hui, L., & Gnedin, N. Y. 1997, *MNRAS*, 292, 27
- Ikeuchi, S., & Ostriker, J. P. 1986, *ApJ*, 301, 522
- Katz, N., Weinberg, D. H., & Hernquist, L. 1996, *ApJS*, 105, 19
- Kim, T.-S., Bolton, J. S., Viel, M., Haehnelt, M. G., & Carswell, R. F. 2007, *MNRAS*, 382, 1657
- Lee, K.-G., et al. 2015, *ApJ*, 799, 196
- Lidz, A., Faucher-Giguère, C.-A., Dall’Aglio, A., McQuinn, M., Fechner, C., Zaldarriaga, M., Hernquist, L., & Dutta, S. 2010, *ApJ*, 718, 199
- Lukić, Z., Stark, C. W., Nugent, P., White, M., Meiksin, A. A., & Almgren, A. 2015, *MNRAS*, 446, 3697
- McDonald, P., Miralda-Escudé, J., Rauch, M., Sargent, W. L. W., Barlow, T. A., & Cen, R. 2001, *ApJ*, 562, 52
- McDonald, P., Miralda-Escudé, J., Rauch, M., Sargent, W. L. W., Barlow, T. A., Cen, R., & Ostriker, J. P. 2000, *ApJ*, 543, 1
- McDonald, P., et al. 2005, *ApJ*, 635, 761
- Meiksin, A., Bryan, G., & Machacek, M. 2001, *MNRAS*, 327, 296
- Meiksin, A., & White, M. 2001, *MNRAS*, 324, 141
- . 2004, *MNRAS*, 350, 1107
- Meiksin, A. A. 2009, *Reviews of Modern Physics*, 81, 1405
- Peebles, P. J. E. 1980, *The large-scale structure of the universe*
- Peeples, M. S., Weinberg, D. H., Davé, R., Fardal, M. A., & Katz, N. 2010a, *MNRAS*, 404, 1281
- . 2010b, *MNRAS*, 404, 1295
- Petitjean, P., Mueket, J. P., & Kates, R. E. 1995, *A&A*, 295, L9
- Pritchard, J. R., & Loeb, A. 2012, *Reports on Progress in Physics*, 75, 086901
- Puchwein, E., Bolton, J. S., Haehnelt, M. G., Madau, P., & Becker, G. D. 2014, arXiv:1410.1531 [astro-ph.CO]
- Puchwein, E., Pfrommer, C., Springel, V., Broderick, A. E., & Chang, P. 2012, *MNRAS*, 423, 149
- Reisenegger, A., & Miralda-Escudé, J. 1995, *ApJ*, 449, 476
- Ricotti, M., Gnedin, N. Y., & Shull, J. M. 2000, *ApJ*, 534, 41
- Rorai, A., Hennawi, J. F., & White, M. 2013, *ApJ*, 775, 81
- Rudie, G. C., Steidel, C. C., & Pettini, M. 2012, *ApJ*, 757, L30
- Schaye, J. 2001, *ApJ*, 559, 507
- Schaye, J., Theuns, T., Rauch, M., Efstathiou, G., & Sargent, W. L. W. 2000, *MNRAS*, 318, 817
- Schaye, J., et al. 2010, *MNRAS*, 402, 1536
- Shull, J. M., France, K., Danforth, C. W., Smith, B., & Tumlinson, J. 2010, *ApJ*, 722, 1312
- Springel, V. 2005, *MNRAS*, 364, 1105
- Springel, V., Yoshida, N., & White, S. D. M. 2001, *New Astron.*, 6, 79
- Syphers, D., & Shull, J. M. 2013, *ApJ*, 765, 119
- Theuns, T., Schaye, J., & Haehnelt, M. G. 2000, *MNRAS*, 315, 600
- Theuns, T., Schaye, J., Zaroubi, S., Kim, T.-S., Tzanavaris, P., & Carswell, B. 2002a, *ApJ*, 567, L103
- Theuns, T., & Zaroubi, S. 2000, *MNRAS*, 317, 989
- Theuns, T., Zaroubi, S., Kim, T.-S., Tzanavaris, P., & Carswell, R. F. 2002b, *MNRAS*, 332, 367
- Tytler, D., Paschos, P., Kirkman, D., Norman, M. L., & Jena, T. 2009, *MNRAS*, 393, 723
- Viel, M., Bolton, J. S., & Haehnelt, M. G. 2009, *MNRAS*, 399, L39
- Viel, M., & Haehnelt, M. G. 2006, *MNRAS*, 365, 231
- Viel, M., Haehnelt, M. G., & Springel, V. 2004, *MNRAS*, 354, 684
- Vogelsberger, M., et al. 2014, *Nature*, 509, 177
- Worseck, G., Prochaska, J. X., Hennawi, J. F., & McQuinn, M. 2014, arXiv:1405.7405 [astro-ph.CO]
- Worseck, G., et al. 2011, *ApJ*, 733, L24
- Zaldarriaga, M., Hui, L., & Tegmark, M. 2001, *ApJ*, 557, 519
- Zhang, Y., Anninos, P., Norman, M. L., & Meiksin, A. 1997, *ApJ*, 485, 496